# Strong, Conductive, Lightweight, Neat Graphene Aerogel Fibers with Aligned Pores

**Zhen Xu,[†] Yuan Zhang,[‡] Peigang Li,[‡] and Chao Gao[†,*]**

[†]MOE Key Laboratory of Macromolecular Synthesis and Functionalization, Department of Polymer Science and Engineering, Zhejiang University, 38 Zheda Road, Hangzhou 310027, People's Republic of China, and [‡]Center for Optoelectronics Materials and Devices, Department of Physics, Zhejiang Sci-Tech University, Hangzhou 310018, People's Republic of China

Since the discovery of graphene by mechanical cleavage in 2004,[1] this new two-dimensional (2D) material has demonstrated numerous exceptional properties that make it attractive for many promising applications, such as nanoelectronic devices, sensors, functional composites, and energy storage.[1−12] However, the poor dispersibility of pristine graphene in common solvents hinders its extensive applications especially for functional nanocomposites and energy storage materials, which unanimously require mass production of well-soluble graphene. To circumvent the limited processability of pristine graphene, graphene oxide (GO) is alternatively manufactured as an important and scalable precursor of graphene and exhibits excellent dispersibility in water and polar organic solvents due to its abundant oxygen-containing functional groups.[5−11] The combination of its good dispersibility and rich chemistry raises a versatile protocol to prepare multifunctional, macroscopic graphene-based materials since GO can be readily converted into reduced graphene (RG) *via* the established chemical or thermal methods.[5−7,11−16]

Recently, the finding of GO liquid crystals (LCs) profoundly promotes macroscopic graphene-based materials to the advanced ones with ordered structure.[17−21] Through simple fluid assembly, the alignment of GO sheets in their LCs aids the effective translation of special attributes of graphene, including high mechanical strength and fine electrical and thermal conductivity, into the resultant macroscopic ordered materials.[18] For example, strong graphene papers made by filtration[22] and continuous solid graphene fibers spun from its LCs[18] or assembled from GO gels[23] have been achieved with the advantages of interior sheet alignment.

**ABSTRACT**
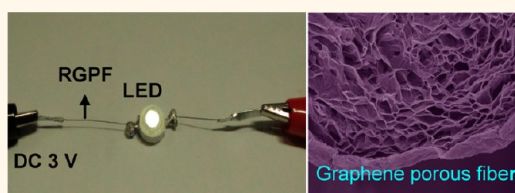


Liquid crystals of anisotropic colloids are of great significance in the preparation of their ordered macroscopic materials, for example, in the cases of carbon nanotubes and graphene. Here, we report a facile and scalable spinning process to prepare neat "core−shell" structured graphene aerogel fibers and three-dimensional cylinders with aligned pores from the flowing liquid crystalline graphene oxide (GO) gels. The uniform alignment of graphene sheets, inheriting the lamellar orders from GO liquid crystals, offers the porous fibers high specific tensile strength (188 kN m$^{-1}$ kg$^{-1}$) and the porous cylinders high compression modulus (3.3 MPa). The porous graphene fibers have high specific surface area up to 884 m$^2$ g$^{-1}$ due to their interconnected pores and exhibit fine electrical conductivity (2.6 × 10$^3$ to 4.9 × 10$^3$ S m$^{-1}$) in the wide temperature range of 5−300 K. The decreasing conductivity with decreasing temperature illustrates a typical semiconducting behavior, and the 3D interconnected network of 2D graphene sheets determines a dual 2D and 3D hopping conduction mechanism. The strong mechanical strength, high porosity, and fine electrical conductivity enable this novel material of ordered graphene aerogels to be greatly useful in versatile catalysts, supercapacitors, flexible batteries and cells, lightweight conductive fibers, and functional textiles.

**KEYWORDS:** liquid crystal · graphene oxide · aligned pores · aerogel · graphene fiber

Aside from the strong solid graphene fibers and films/papers with compactly stacked structures, three-dimensional (3D) assembled lightweight graphene aerogels with high porosity are of particular significance for energy storage (*e.g.*, chemical supercapacitors and hydrogen storage) and catalyst beds.[24−30] From the GO precursor, there are two main emerging strategies to obtain graphene aerogels: self-assembly during reduction[24−27] and freeze-drying followed by reduction.[28−30] Adopting the first strategy,

Shi and co-workers prepared graphene aerogel and revealed its promising use as a chemical super-capacitor;[24] Wang and co-workers exploited metal-ion-promoted assembly to obtain noble metal hybridized graphene aerogel and used it as a catalyst.[26] Alternatively, Wang and Ellsworth invented the freeze-drying process followed by reduction to prepare graphene aerogels,[28] and Wang et al. further utilized this method to get graphene/Nafion composite aerogels functionalized by platinum nanoclusters.[29] Generally, the disordered architecture featured by randomly interconnected GO or RG sheets results in deficient electrical conductivity and limited mechanical strength. Hence, accessing the ideal material of light-weight graphene aerogel with strong mechanical performance, high surface area, and fine electrical conductivity is still a big challenge hitherto.

To resolve such an important issue, we anticipate that the intrinsic ordering of GO LCs should favor the simultaneous improvement in both mechanical strength and electrical conductivity of the graphene-based porous materials, inspired by the prominent properties of solid graphene fibers composed of aligned graphene sheets.[18] Moreover, the fluid nature of GO LCs facilitates the production of continuous ordered graphene aerogels, which has never been achieved previously. Here, for the first time, we prepared continuous neat GO aerogel fibers with unique "porous core–dense shell" structure from flowing GO LCs with lamellar ordering by the combination of spinning technology and ice-templating strategy. The resultant macroscopic assembled materials hold high tensile strength and high compression strength because of the interior uniform alignment of GO sheets. After chemical reduction and annealing process, the aligned porous graphene fibers possess high specific surface area and fine electrical conductivity. In this context, we solved this widely expressed conflict between high porosity (meaning lightweight and high surface area) and high performance in both strength and electrical conductivity, which could be helpful in the future design and fabrication of advanced aerogel materials.

## RESULTS AND DISCUSSION

We synthesized GO by modified Hummers method[31] from natural graphite and got exfoliated single-layered GO sheets in their aqueous dispersions under mild ultrasonication at 40 kHz for 30 min, according to our previous process.[17,18] As shown in atomic force microscopy (AFM) images (Figure 1a and Figure S1 in Supporting Information), GO sheets deposited on a mica substrate are measured as thick as ∼0.8 nm ($t$), with an average lateral width ($w$) ∼2.0 $\mu$m, demonstrating the complete exfoliation in water. The atomic thickness and micrometer-scale width of GO sheets imply their high aspect ratio ($w/t > 2000$), and this
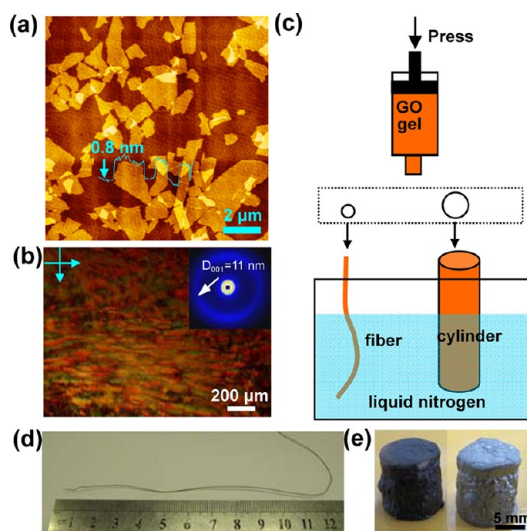


Figure 1. (a) AFM image of GO sheets deposited on mica. (b) Representative POM microscopic image of GO gel with $f_m$ 10.1% between crossed polarizers, and the inset is the 2D SAXS pattern of the gel. (c) Scheme for preparation of GO porous fibers (GOPFs) and GO porous cylinders (GOPCs). Photographs of GOPF (d), GOPC (e, left), and RGPC (e, right).

highly asymmetrical nature determines the spontaneous formation of lyotropic LCs, from nematic phase to a lamellar one, with increasing GO concentration.[17,18]

Subsequently, we prepared concentrated liquid crystalline GO gels with lamellar structure. Under polarized optical microscopy (POM), the GO gel loaded in a planar cell shows vivid banded textures between crossed polarizers (Figure 1b), which is a typical lamellar optical texture with line disclinations.[18] The quantitative lamellar structural information was derived from synchronous small-angle X-ray scattering (SAXS) tests. The two-dimensional SAXS pattern of GO gel (mass fraction $f_m$, 10.1%, corresponds to volume fraction $\phi$, 7.1%) shows a distinct scattering loop (Figure 1b, inset), indicating a lamellar structural character in the powder GO gel at rest. From the scattering profile in Figure S2, the lamellar spacing ($d_s$) between neighboring GO sheets is measured as 11.2 nm. According to the 1D swelling model for sheet-shaped colloids, the layer spacing can be calculated as $d_s = t/\phi$ ($t = 0.8$ nm).[18,32,33] In the case of concentrated GO gel, the theoretical spacing is derived to be 11.3 nm, almost equal to the experimental value (11.2 nm) obtained from the SAXS test, demonstrating the monolayer characteristic for the GO sheets in the whole hydrogel.

The lamellar structure of GO liquid crystalline gel has previously prompted the fabrication of neat GO solid fibers in which GO sheets stack densely.[18] Considering that freeze-drying is a prevailing strategy to prepare conventional aerosols from nanoparticles or polymer solutions,[28−30,34−37] the marriage of freeze-drying technology and GO LCs would possibly give birth to macroscopically assembled GO fibers with aligned pores,
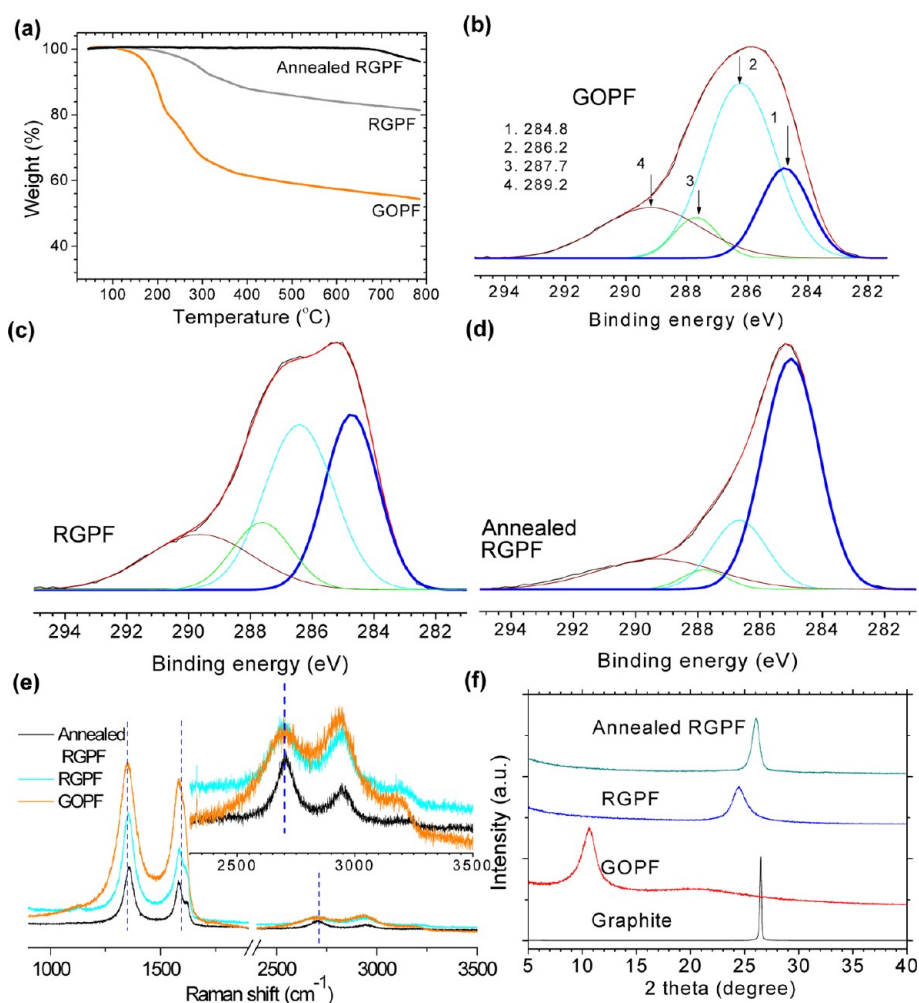
**Figure 2.** TGA curves (a), XPS spectra (b—d), Raman spectra (e), and XRD patterns (f) of GOPF, RGPF, and annealed RGPF.

an essentially different structure from the solid GO fibers made by the coagulant process.[18] In fact, conducting the process depicted in Figure 1c, we prepared continuous GO porous fibers (GOPFs) by extruding GO LC gels into liquid nitrogen followed by freeze-drying. In the spinning of GOPFs, two main factors determine the continuity of aerogel fibers: the concentration of GO gel and the diameter of the nozzle. We found that GO gels with low concentrations (for example, $f_m$ ~6.0% in the case of nozzle with diameter 60 $\mu$m) were prone to deform into droplets at the end of nozzle and cannot support the form of fibers in the gel state (see photograph in Figure S3). Conversely, the larger diameters of nozzles match GO gels with lower concentrations to keep the continuity of fibers. In this study, we chose the concentrated GO gel at $f_m$ ~10.1% and the diameter of spinning nozzles was tuned from 60 $\mu$m to 1 cm. Accordingly, we obtained a series of GOPFs with controllable diameters. Figure 1d,e give examples of GOPF ~100 $\mu$m in diameter and cut GO porous cylinders (GOPC) ~1 cm in diameter, respectively.

It is known that the insulating GO can be easily converted to conductive graphene by either chemical or thermal reduction.[5−7,11] Herein, we obtained reduced

graphene porous fibers (RGPFs) or reduced graphene porous cylinders (RGPCs) by chemical reduction of GOPFs or GOPCs using hydroiodic acid aqueous solution as the reducing reagent.[18,38] After chemical/thermal reduction, the dull black appearances of GOPFs and GOPCs turn to metal luster of RGPFs and RGPCs (Figure 1e). In the chemical/thermal reduction process, there are two chemical structural evolutions: the elimination of pendant oxygen-containing functional groups such as hydroxyl and epoxy groups and the restoration of conjugated carbon net, which are proven by the detailed characterizations of thermogravimetric analysis (TGA), X-ray photoelectron spectroscopy (XPS), and Raman spectroscopy (Figure 2). In TGA curves (Figure 2a), the weight losses before 350 °C of GOPF, RGPF, and annealed RGPF are measured as 36.1, 9.6, and almost 0%, respectively. The dramatic decreasing of weight loss is ascribed to the elimination of functional groups in the stepwise reduction, and accordingly, the density of GOPF (110 ± 2 mg cm$^{-3}$) decreases to 71 ± 3 mg cm$^{-3}$ of RGPF and 56 ± 3 mg cm$^{-3}$ of annealed RGPF. Figure 2b−d and Figure S4 show the XPS survey spectra of GOPF, RGPF, and annealed RGPF, and the atomic ratios of C1s/O1s increase
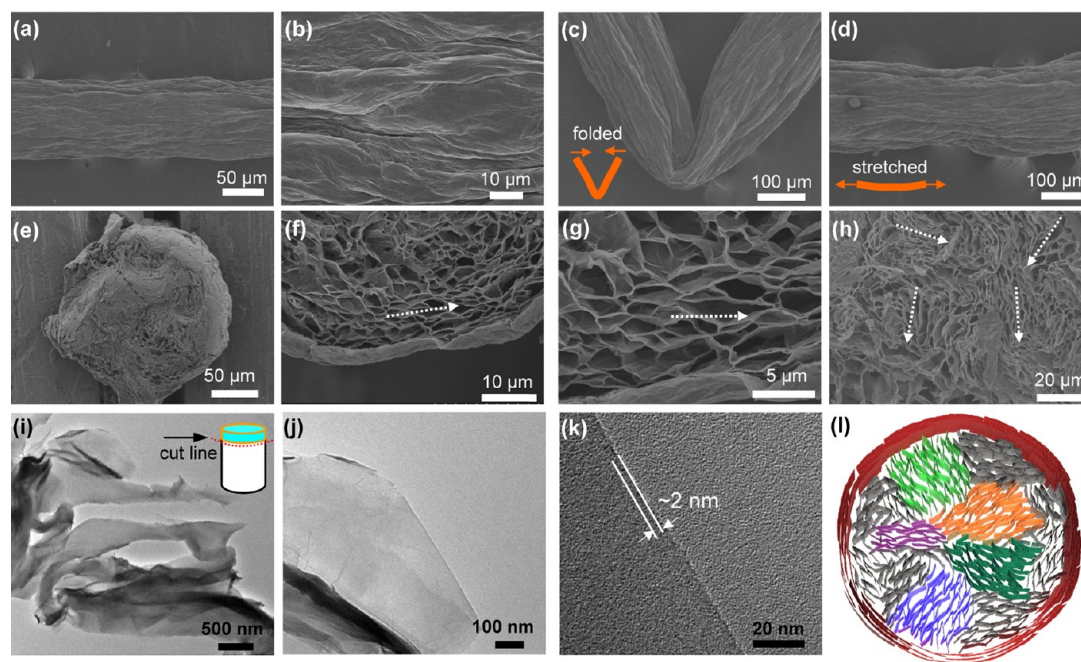
**Figure 3.** SEM images of the surface of RGPF (a,b) and folded/stretched RGPF (c,d). (e—h) SEM images of fracture morphology of RGPF. The arrows indicate the alignment direction of RG sheets. (i—k) TEM images of fractured RGPF embedded in the epoxy resin. The inset in (i) shows how to prepare TEM samples by cryo-cutting. (l) Schematic core—shell structure model for RGPFs and GOPFs. Regions of different colors represent GO lamellar regions with different director vectors in the core, and the red color denotes the dense shell.

from 3.2 to 5.3 and 13.3 for GOPF, RGPF, and annealed RGPF. In their XPS C1s spectra, four peaks centered at 284.8, 286.2, 287.7, and 289.2 eV (Figure 2b—d) are assigned to C—C/C═C in aromatic rings, C—O (epoxy), carbonyl (C═O), and carboxyl (COO) groups, respectively.[11,38] In comparison of these three XPS spectra, the peak intensity at 284.8 eV stepwisely becomes stronger from GOPF to RGPF and annealed RGPF, together with the fading of peaks at 286.2, 287.7, and 289.2 eV, verifying the removal of oxygen functional groups and the simultaneous restoration of conjugated network. This chemical evolution is also confirmed by the increasing intensity of the 2D band at 2680 cm$^{-1}$ in their Raman spectra (Figure 2e).[11,12,18,38] In X-ray powder diffraction (XRD) analysis (Figure 2f), the elimination of functional groups leads to the decreasing of interlayer spacing, from 0.828 nm of GOPF to 0.363 nm of RGPF and 0.342 nm of annealed RGPF. The annealed sample shows a sharper peak in the XRD pattern, revealing more regular packing of RG sheets with a longer correlation length.

To observe the architecture of graphene porous fibers, scanning electron microscopy (SEM) and transmission electron microscopy (TEM) characterizations were used. We found that graphene sheets stacked densely to form a wrinkled shell surface, and graphene sheets interconnected to form a porous part which is surrounded by the dense shell. The wrinkles could be ascribed to graphene sheet surfaces and interconnecting graphene sheet boundaries. The alignment of graphene sheets along the fiber axis originates from the confined alignment at the interface between

flowing GO gel and the nozzle.[39] Interestingly, RGPFs have fine flexibility and can be folded (for example, to a 60° angle shape in Figure 3c), and the bent fiber can be stretched to its original straight shape without any fracture (Figure 3d).

In the porous core of RGPF, RG sheets interconnect each other and align along the axial direction, forming axially aligned empty cells with a width of about 2—5 $\mu$m, as shown in the fractured SEM images of RGPF (Figure 3e—h). Such a loosely porous structure in the core is utterly different from the compact stacking structure of the shell. Besides the effect of axial direction freezing, we concluded that the primary reason for the aligned porous fibers is the fine orderings in the original lamellar liquid crystalline GO gels flowed in the capillary. Although there are different aligned directions for assembled walls of graphene sheets in the fracture (Figure 3h), the vectors of graphene sheets (normal to the sheet plane) are vertical to the fiber axis (i.e., the flowing direction) to form the aligned pores. To examine the atomic structure of porous cell walls, we used fracture TEM characterization by cutting RGPF embedded in the epoxy resin. The ribbon-like graphene sheets in Figure 3i are the cut strips of porous cell walls in RGPF, and high-resolution TEM images (Figure 3j,k) show that the thickness of the strips is about 2 nm (3—5 layers graphene), suggesting that the porous cell walls consist of stacked graphene sheets in few layers. These microscopy observations help us to depict the structural model of our aligned porous graphene fibers (Figure 3l). The outer dense shell wraps
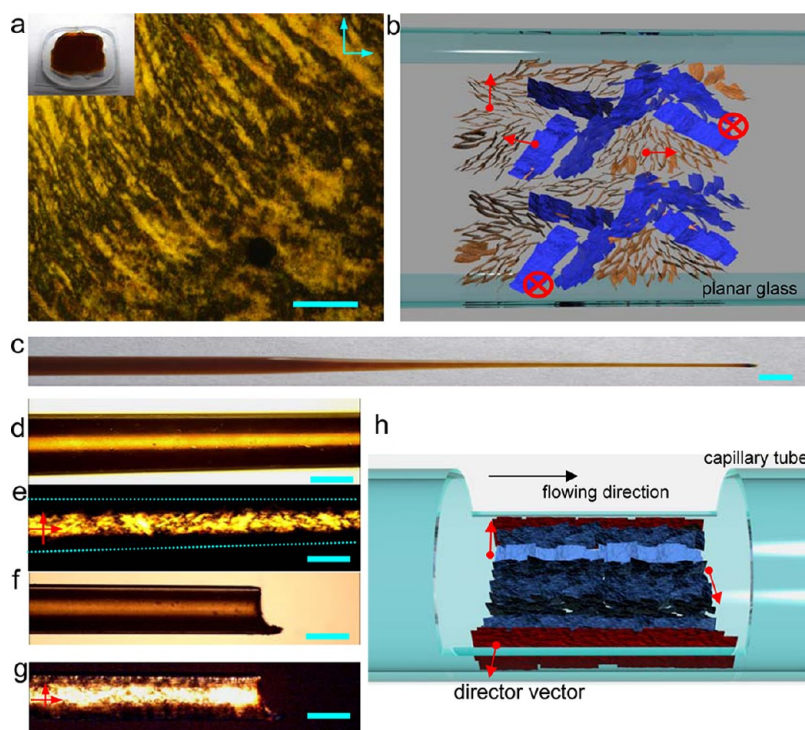
**Figure 4.** (a) POM image of the resting powder GO gel between crossed polarizers. The inset is a photo of the resting GO LC gel loaded in a planar cell. (b) Structural model of the resting powder GO LC gel. The arrows and the cross indicate director vectors on and into the observation plane, respectively. (c) Photo of flowing GO gel in a capillary tube. (d,f) Optical microscopic images of flowing GO gel in a capillary tube at different sections. (e,g) POM images between crossed polarizers corresponding to panels e and f, respectively. (h) Structural model of flowing GO liquid crystalline gel with flow-induced alignments of GO sheets, indicating the formation of core−shell structure under confined flowing. All of the vectors are identically perpendicular to the capillary surface. Scale bars are (a,d−g) 200 $\mu$m and (c) 1 cm.

the inner porous core to form the core−shell structure. Graphene sheets, not only in the dense shell but also in the porous core, have a uniform alignment along the fiber axis. Such a uniform alignment of graphene sheets would favor the mechanical strength of assembled fibers in the axial direction.

The following question arises: how does this interesting core−shell structure form with the uniform alignment? The fluid of anisotropic colloids (2D GO sheets in our case) is a typical shear flow, and the constituent colloids are prone to align along the flowing direction. This phenomenon has been observed in the liquid crystalline systems of 2D colloids including GO sheets and 1D colloids (carbon nanotubes, CNTs) and ever used to make ordered materials.[17,40−43] To truly understand the alignment of GO sheets in the spinning process, we took POM observations on GO gels at the both resting state and flowing state, as shown in Figure 4. The POM image (Figure 4a) together with the aforementioned SAXS results (Figures 1b and S2) demonstrates that GO gel in the resting state is a powder LC that contains lamellar ordered domains separated by plentiful line disclinations (Figure 4b). Once GO gel flows, the alignment of the GO sheets complies with the flowing direction along the capillary tube, and the corresponding POM images exhibit uniform birefringence between crossed polarizers

(Figure 4d−g). This inspection under POM illustrates the uniform alignments of GO sheets, of which all of the director vectors are identically perpendicular to the capillary surface. A closer look at the neighboring region of the inner capillary surface shows that the surface tension causes GO sheets to form lamellar arrays parallel to the surface, which are widely observed in the preparation of GO papers by solution casting.[5,12,21] In other words, the GO sheet-assembled tube-like shell forms dynamically with the "templating" of the inside wall of the spinning tube. Therefore, after fast freezing in liquid nitrogen and sublimation of the contained water, the ordered structure of flowing GO gel is fixed and the core−shell structure is preserved in the dried GOPFs.

The porosity of our graphene aerogel fibers was investigated by nitrogen sorption characterization. The type IV nitrogen adsorption/desorption isotherm of aerogel fiber shows a hysteresis loop at high relative pressure, indicating the existence of plentiful mesopores in the aerogel (Figure 5a). According to the Barrett−Joyner−Halenda (BJH) method, much of the pore volume (5.85 cm$^3$ g$^{-1}$) lies in the 3.4−100 nm range for the pore size distribution, with two sharp peaks at 3.8 nm and a broad one at 9.5 nm (Figure 5b and Figure S5). The broad pore size distribution, spanning from several to 100 nm, implies that the aerogel
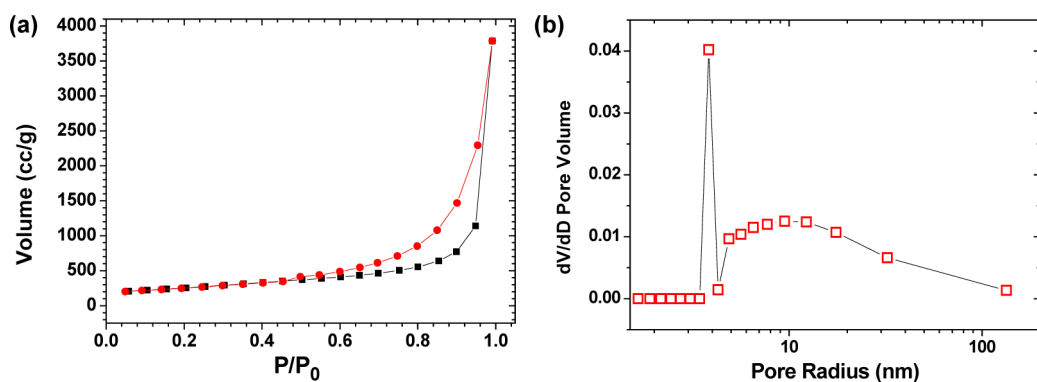
**Figure 5.** (a) Nitrogen adsorption (circle) and desorption (square) isotherms of annealed RGPF. (b) BJH (Barrett—Joyner—Halenda) desorption pore size distribution of annealed RGPF.

fiber is rich in the hierarchical pores. From the SEM inspection of the aerogel fiber (Figure 3), the macropores could originate from the interconnected hollow space and the mesopores could be generated by the wrinkled morphology of RG sheets. It is noteworthy that the BET surface area for the aerogel fiber is very high, up to 884 m$^2$ g$^{-1}$, about one-third of the theoretical surface area of monolayer graphene (2600 m$^2$ g$^{-1}$). This high value corresponds to an average number of graphene layers of ~3, which agrees with the TEM observation of the thickness of aligned walls (about 2 nm in Figure 3k). As far as we know, the specific surface area of our graphene aerogel fibers is the highest value for graphene aerogels reported so far, which is a little higher than that of graphene 3D network fabricated by the chemical vapor deposition (CVD) method (850 m$^2$ g$^{-1}$)[44] and much higher than the values of graphene aerogels prepared by supercritical $CO_2$ drying (512 m$^2$ g$^{-1}$),[25] assembled graphene tapes (400 m$^2$ g$^{-1}$),[45] and CNT aerogels (typically 300—400 m$^2$ g$^{-1}$).[46] The surface area of our neat porous fibers is even approaching that of mesoporous silica-sandwiched graphene composites (980 m$^2$ g$^{-1}$).[47] The hierarchically porous structure of our aerogel fibers with very broad pore distribution is likely in favor of their high surface area. In addition, there might be part of single-layer graphene sheet in the porous structures.

The attribute of high surface area generally conflicts with good mechanical property of materials in the disordered system. So the ideal materials with both merits have rarely been accessed previously, nevertheless, they could be realized in our ordered system. Mechanical tensile measurements demonstrate that both GOPFs and RGPFs exhibit typical plastic deformation under tensile loading at room temperature (Figure 6). The initiating regions in tensile curves are possibly a result from the stretching of the wrinkled GO and RG sheets, with Young's moduli of 270 MPa for GOPFs and 350 MPa for RGPFs. Upon further straining, GOPFs and RGPFs show typical fracture strengths of 6.9 and 11.1 MPa, at ultimate elongations of 4.5 and 6.2%,
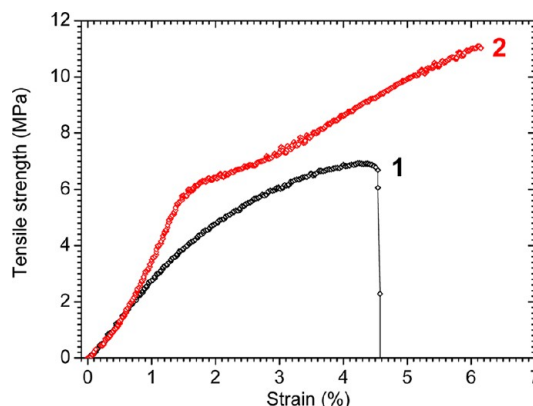


**Figure 6.** Typical mechanical measurements under tensile loading for GOPF (curve 1) and RGPF (curve 2). The Young's moduli of GOPF and RGPF at low deformation are 270 and 350 MPa, respectively.

respectively. The superior Young's modulus and fracture strength for RGPFs could probably be attributed to more compact stacking of graphene sheets resulting from smaller interlayer spacing after reducing GO (Figure 2f).[12,18,38] Compared with graphene tapes (about 25 kN m kg$^{-1}$ of specific strength at 0.5% ultimate elongation),[45] our porous fibers have much higher specific strength up to 188 kN m kg$^{-1}$ with an order of magnitude higher break elongation (6.2%). The specific strength of our porous fibers is even comparable to that of a commercial aluminum/manganese alloy (~222 kN m kg$^{-1}$). The unique "porous core—dense shell" structure with aligned graphene building blocks is likely responsible for the high strength of graphene porous fibers.

The plastic deformation of GOPFs and RGPFs involves two stages of stretching and displacement, which is similar to the cases of spun graphene[18] and CNT fibers.[43] Representative SEM images regarding RGPF fracture morphology are shown in Figure 7a—f. Figure 7a,b gives a panorama of the fracture surface with a certain elongation, implying the elastic breakage nature of RGPF under tension. At high magnification, the typical stretched fibrils at fracture tips (Figure 7c) and distinct displacement lines of slide
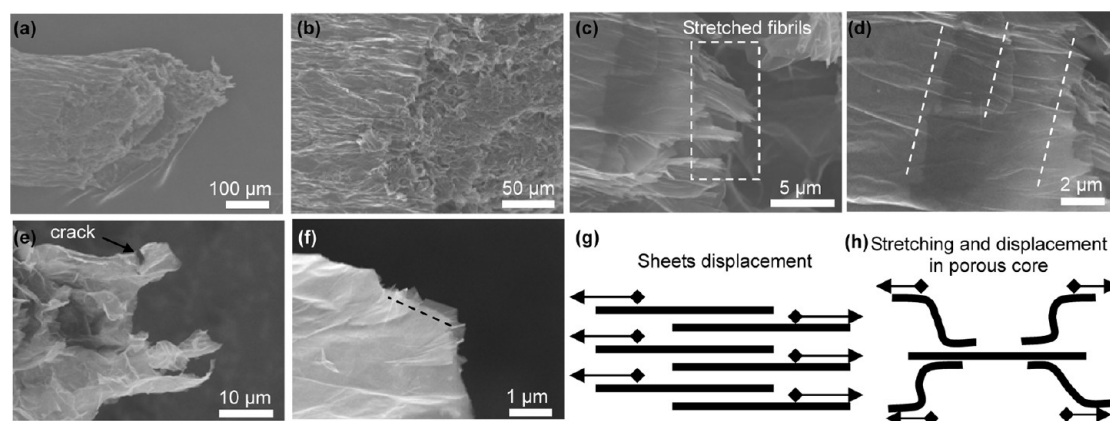
**Figure 7.** SEM images of RGPF surface (a,b) and failure morphology after tensile test (c,d). The lines in panels d and f indicate the slide lines of RG sheets. The deformation mechanism models of the shell (g) and the porous part (h) in RGPF; the black lines represent RG sheets in RGPF.

graphene sheets illuminate the stretching and displacement mechanisms, respectively. Additionally, some cracks can be observed in the fracture tips (Figure 7e), with displacements as well (Figure 7f). On the basis of the core–shell structure of RGPFs, we speculate that the dominating deformation in the dense shell is sheet displacement, and both stretching and displacement deformations simultaneously work in the porous core. The corresponding deformation models are depicted in Figure 7g,h, respectively.

The porous cylinders also have core–shell structure, and the alignment of graphene sheets should also impart fine compression strength to the macroscopic assembled materials. Because of the strong compression strength in the diametrical direction, the porous cylinders (GOPCs, RGPCs, and annealed RGPCs) are able to completely keep the circle shape of the section after cutting (Figure 8a,b and Figure S6). In the images of the sections, we can identify that aligned GO and RG sheets are uniformly vertical to the section surfaces in the core, similar to the section morphology of porous fibers (Figure 3e,f).

Under compression in the axial direction, GOPCs and RGPCs exhibit elastic–plastic deformation.[24,25] The compressive curves (Figure 8d) are divided into three regimes: linear elasticity at low stress (regime 1), long plasticity (regime 2), and densification (regime 3). The uniform alignment of graphene in the compressive direction is responsible for the very short linear elasticity regime (<3%) and imparts high compression strength to the ordered porous materials. The GOPC has a high compression modulus of 1.1 MPa. Notably, the compression modulus of RGPC with a density as low as 71 mg cm$^{-3}$ even rises to 3.3 MPa (Figure 8d), around 1 order of magnitude higher than that of graphene aerogels without sheet alignment (390 kPa).[24] The RGPC is also comparable to graphene aerogels with similar density made by supercritical $CO_2$ drying with compression modulus of 2.8 MPa that is around 5 times higher than the common freeze-dried graphene
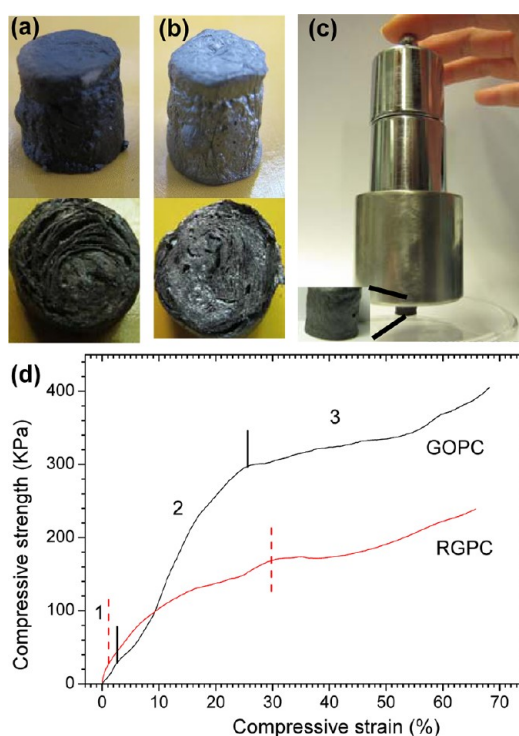


**Figure 8.** (a) Photographs of GOPC (top) and the section plane after cutting (bottom). (b) Photographs of RGPC (top) and the section plane (bottom). (c) Photograph of 42 mg GOPC lifting 900 g poise. (d) Compression stress–strain curves of GOPC and RGPC at different set stains; 1, 2, and 3 represent three deformation regimes: linear elasticity, plastic, and densification, in succession.

aerogels.[25] In fact, the GOPC can support a weight more than 20 000 times its own weight without breakage (Figure 8c, 42 mg GOPC lifts 900 g poise). Again, such high compression strength is ascribed to the core–shell structure constructed with well-aligned graphene sheets. SEM observations on the deformation of RGPCs under pressure and the proposed deformation mechanism are given in Figure S7.

After chemical reduction, GOPFs and GOPCs turned from insulator to electrically conductive RGPFs and
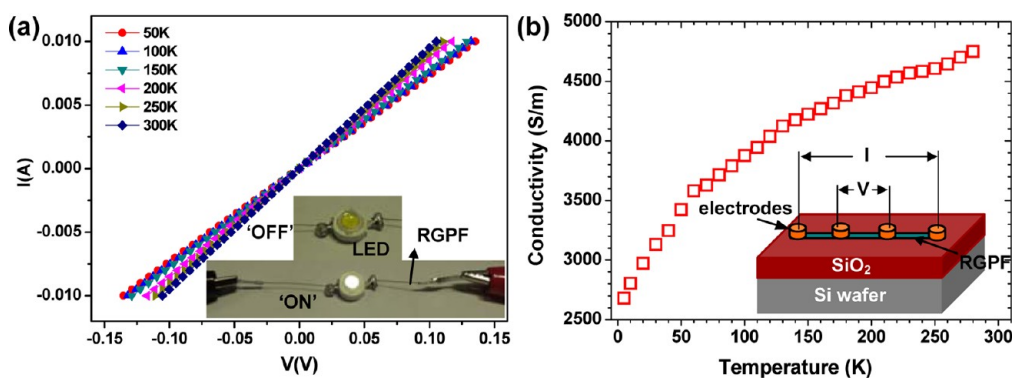
**Figure 9.** (a) $I-V$ curves of annealed RGPF measured by four-probe method in the temperature range of $5-300$ K. The inset is a constructed circuit using RGPF as lightweight conductive wire. (b) Plot of temperature-dependent conductivity of annealed RGPF. The inset is the sketched four-probe apparatus of the conduction test.

RGPCs. RGPFs and annealed RGPFs show electrical conductivities of $2.0 \times 10^3$ and $4.9 \times 10^3$ S m$^{-1}$, respectively, due to the restoration of the conjugated network in RG sheets. The conductivity of our graphene porous fibers is more than 1 order of magnitude higher than that of *in situ* self-assembled graphene aerogel (87 S m$^{-1}$)[24] or cross-linked graphene aerogel ($1 \times 10^2$ S m$^{-1}$),[30] more than 3 orders of magnitude higher than graphene—polymer composite aerogel (1 S m$^{-1}$),[29] even higher than that of 3D interconnected neat graphene networks prepared by CVD ($1 \times 10^3$ S m$^{-1}$).[44] Likewise, the high conductivity of our RGPFs is attributed to the fine alignment of graphene sheets and the densely packed shell in the core—shell assembled structure. Notably, the conductivity of RGPF is stable after 100 bending cycles (Figure S8). To show the fine conductivity of the whole fiber, rather than selected segments, we used porous graphene fibers to construct a circuit. A LED lamp can be highly illuminated at 3 V (Figure 9a, inset), showing that the porous fibers can be used as lightweight conductive wires or cables in electrical applications.

To further study the electrical transport properties of our neat graphene fibers, we investigated the temperature ($T$)-dependent conductivity of annealed RGPF in the $5-300$ K range. The inverse slopes of $I-V$ curves in Figure 9a denote the resistances ($\sigma$) of the annealed RGPF sample, and its conductivity increases from $2.6 \times 10^3$ S m$^{-1}$ at 5 K to $4.9 \times 10^3$ S m$^{-1}$ at 290 K, as shown in Figure 9b. This temperature-dependent conductivity suggests the semiconducting behavior of RGPF, possibly because of the existence of point defects in graphene and contacting band gap among interconnected graphene sheets.[48] Theoretically, two main models are developed to explain the conducting mechanism of the semiconductor: (i) hopping mechanism with a resistance temperature function $\ln \sigma \propto T^{-1/4}$, and (ii) tunneling conduction mechanism obeying a function $\ln \sigma \propto T^{-1/2}$.[49] For the annealed RGPFs, the function $\ln \sigma \propto T^{-1/4}$ fits linearity better than $\ln \sigma \propto T^{-1/2}$ (the fitting lines are shown in Figure S9), indicating that the electrical conduction is possibly controlled by the hopping mechanism, similar to the case of CNTs.[48] In the frame of Mott's hopping model, the relationship between resistance and temperature can be expressed as $\ln \sigma \propto T^{-[1/(d+1)]}$, where $d$ is the dimensionality.[50] As shown in Figure S9, the curves of $\ln \sigma$ *versus* $T$ are linearly fitted to three ($d = 3$), two ($d = 2$), and one dimension ($d = 1$), holding coefficients of determination of 0.982, 0.971, and 0.951, respectively. This result further suggests that the transport in the graphene aerogel could obey three- and two-dimensional hopping mechanisms simultaneously.[51] The two-dimensional nature of the single graphene sheet and interconnected graphene network in graphene aerogel fibers could explain this dual conducting behavior. On the other hand, the temperature-dependent conductivity results demonstrated very high electrical conductivity of graphene aerogel fibers at very low temperature, which could be useful in promising lightweight conductive wires working at ultimate low temperature.

The aligned pores in graphene aerogel fibers provide smooth channels for mass transferring, and diverse additives such as polymers, ions, and other guest compounds could easily infiltrate into the aligned pores to get multifunctional composite fibers. For instance, we prepared graphene—SBS composite fibers contaning ~80 wt % SBS, which exhibited high electrical conductivity of $1.5 \times 10^3$ S m$^{-1}$, close to that of RGPF ($2.0 \times 10^3$ S m$^{-1}$). This implies that the infiltration of polymer has little influence on the connected conductive graphene network,[43] similar to the CNT aerogel composites.[49,52,53] In addition, we prepared graphene porous fibers deposited with silver and platinum nanoclusters, through adsorption of metal ions followed by *in situ* reduction. Because of the connectivity of pores, the Ag or Pt nanocrystals decorated evenly not only on the fiber outer surface but also on the inner pore walls (Figure S10), promising their applications as catalysts[26,29,54,55] and for energy storage.[24,25]

## CONCLUSIONS

In summary, we have prepared aligned porous graphene fibers/cylinders by spinning the liquid

crystalline GO gels into liquid nitrogen. The porous fibers have unique core—shell structure, with uniform alignment of GO or RG sheets inherited from the lamellar orders in the flowing dope of GO liquid crystals. The hierarchical porosity gives the graphene aerogel fibers high surface area, affording a simple and effective way to prepare multifunctional fibers composed of aligned graphene sheets. The ordered structure confers high tensile and compression strengths on GO and RG porous fibers and bestows fine electrical conductivity on RG fibers. Because of their excellent integrated properties, the aligned porous graphene fibers and three-dimensional cylinders offer promising applications in lightweight conductive cables, energy storage, catalysts, and functional textiles. The unique core—shell structure with well-aligned pores makes the seemingly contradictory attributes of high porosity and good mechanical/electrical properties perfectly harmonious, paving the way to design and fabricate lightweight porous materials with high performances.

## EXPERIMENTAL METHODS

**Materials.** Graphite powder (40 $\mu$m) was obtained from Qingdao Henglide Graphite Co., Ltd. Concentrated $H_2SO_4$ (98%), $KMnO_4$, HI acid (40%), $AgNO_3$, and $H_2PtCl_6 \cdot 6H_2O$ were purchased from Sinopharm Chemical Reagent Co., Ltd., and used as received.

**Synthesis of GO.** Graphene oxide was synthesized according to the process we reported before.[17,18]

**Preparation of Graphene Oxide Porous Fibers (GOPFs) and Reduced Graphene Porous Fibers (RGPFs).** Liquid crystalline GO gel was prepared by centrifugation of GO dispersion at high speed (17 500 rpm). The prepared GO gel was loaded into the home-made spinning apparatus equipped with a switchable nozzle with tunable diameters. The GO gel was continuously injected into liquid nitrogen, and the frozen fibers were transferred into the next freeze-drying (at −60 °C for 2 days) and further vacuum drying (at 60 °C for 24 h) to get GOPFs. As the nozzle diameters are in the millimeter scale, the resulting thick GO "fibers" were coined as porous cylinders (GOPCs).

The RGPFs (or reduced graphene porous cylinders, RGPCs) were prepared by chemical reduction of as-prepared GOPFs (GOPCs) in the aqueous solution of hydroiodic acid (40%) at 80 °C for 8 h,[18,38] followed by washing with methanol and vacuum drying for 12 h. RGPFs (or RGPCs) were further thermally annealed at 1100 °C for 2 h to obtain annealed RGPFs (or RGPCs).

**Preparation of Ag (or Pt)-Hybridized RGPFs and Poly(styrene butadiene styrene) (SBS)—RGPF Composites.** The RGPFs (RGPCs) were immersed in the 10 mL of 0.1 M aqueous solution of $AgNO_3$ (or $H_2PtCl_6$) for 12 h, until the solution infiltrated into its pores. Then, 2 mL of 0.5 M $NaBH_4$ aqueous solution was introduced, and the mixture was heated to 60 °C and kept for 10 min. The fiber was picked up and washed by water three times, followed by vacuum drying at 60 °C for 12 h, and we got the hybridized RGPFs (RGPCs) finally. The SBS complexed RGPFs were prepared by immersing RGPFs into the chloroform solution of SBS (20 wt %) for 24 h. After vacuum drying at 60 °C for 12 h, we got the SBS—RGPF composite fibers.

**Characterization.** AFM images of GO sheets were taken in the tapping mode, carried out on a NSK SPI3800, with samples prepared by spin-coating from diluted aqueous solutions onto freshly exfoliated mica substrates at 1000 rpm. SEM images were taken on a Hitachi S4800 field-emission SEM system. Fractured TEM samples were prepared by embedding the RGPF in the epoxy resin, cutting the fiber on a Power Tome PC, and transferring the sliced sample to the copper grid. TEM images were taken on a Tecnai G2F30 with an accelerating voltage of 300 kV or a JEM-1230 (80 kV). Synchronous SAXS tests were carried out in Shanghai Synchrotron Radiation Facility (SSRF), by using a fixed wavelength of 0.124 nm, a sample to detector distance of 5 m, and an exposure time of 300 s. The scattering patterns were collected on a CCD camera. POM observations were performed with a Nikon E600POL. All electrical transport properties were measured using standard four-probe method on a homemade electrical transport properties measurement system composed of a Keithley 2400 multiple-function source-meter and a Lakeshore low-temperature system. Tensile and compression tests were carried on a HS-3002C at a loading rate of 1 mm/min. XPS was performed using a PHI 5000C ESCA system operated at 14.0 kV. All binding energies were referenced to the C1s neutral carbon peak at 284.8 eV. Nitrogen sorption measurements were performed on a Quantachrome Autosorb-1-c. Before measurement, the sample was outgassed under vacuum at 300 °C for 10 h. TGA was carried out using a thermogravimetric analyzer (PerkinElmer Pyris 1) from room temperature to 800 at 10 °C/min heating rates under $N_2$ atomsphere. XRD data were collected with an X'Pert Pro (PANalytical) diffractometer using monochromatic Cu K$\alpha$1 radiation ($\lambda$ = 1.5406 Å) at 40 kV. Raman spectra were recorded on a Labram HRUV spectrometer operating at 632.8 nm.

*Conflict of Interest:* The authors declare no competing financial interest.

*Supporting Information Available:* AFM images of GO, SAXS scattering profiles of GO LC, XPS spectra of GOPF and RGPF, SEM images of RGPC after compression test, POM images of resting and flowing GO LC gels, linear fitting between conductivity and temperature, and SEM images of Ag and Pt nanocrystal-decorated RGPF. This material is available free of charge *via* the Internet at http://pubs.acs.org.

## REFERENCES AND NOTES

1. Novoselov, K. S.; Geim, A. K.; Morozov, S. V.; Jiang, D.; Zhang, Y.; Dubonos, S. V.; Grigorieva, I. V.; Filrsov, A. A. Electric Field Effect in Atomically Thin Carbon Films. *Science* **2004**, *306*, 666–669.
2. Geim, A. K. Graphene: Status and Prospects. *Science* **2009**, *324*, 1530–1534.
3. Rao, C. N. R.; Sood, A. K.; Subrahmanyam, K. S.; Govindaraj, A. Graphene: The New Two-Dimensional Nanomaterial. *Angew. Chem., Int. Ed.* **2009**, *48*, 7752–7777.
4. Allen, M. J.; Tung, V. C.; Kaner, R. B. Honeycomb Carbon: A Review of Graphene. *Chem. Rev.* **2010**, *110*, 132–145.
5. Zhu, Y. W.; Murali, S.; Cai, W. W.; Li, X. S.; Suk, J. W.; Potts, J. R.; Ruoff, R. S. Graphene and Graphene Oxide: Synthesis, Properties, and Applications. *Adv. Mater.* **2010**, *22*, 3906–3924.
6. Bai, H.; Li, C.; Shi, G. Q. Functional Composite Materials Based on Chemically Converted Graphene. *Adv. Mater.* **2011**, *23*, 1089–1115.
7. Huang, X.; Qi, X. Y.; Boey, F.; Zhang, H. Graphene-Based Composites. *Chem. Soc. Rev.* **2012**, *41*, 666–686.
8. Wu, D. Q.; Zhang, F.; Liu, P.; Feng, X. L. Two-Dimensional Nanocomposites Based on Chemically Modified Graphene. *Chem.—Eur. J.* **2011**, *17*, 10804–10812.

9. Wan, X. J.; Huang, Y.; Chen, Y. S. Focusing on Energy and Optoelectronic Applications: A Journey for Graphene and Graphene Oxide at Large Scale. *Acc. Chem. Res.* **2012**, *45*, 598–607.

10. Park, S.; Ruoff, R. S. Chemical Methods for the Production of Graphenes. *Nat. Nanotechnol.* **2009**, *4*, 217–224.

11. Dreyer, D. R.; Park, S.; Bielawski, C. W.; Ruoff, R. S. The Chemistry of Graphene Oxide. *Chem. Soc. Rev.* **2010**, *39*, 228–240.

12. Compton, O. C.; Nguyen, S. T. Graphene Oxide, Highly Reduced Graphene Oxide, and Graphene: Versatile Building Blocks for Carbon-Based Materials. *Small* **2010**, *6*, 711–723.

13. Li, D.; Muller, M. B.; Gilje, S.; Kaner, R. B.; Wallace, G. G. Processable Aqueous Dispersions of Graphene Nanosheets. *Nat. Nanotechnol.* **2008**, *3*, 101–105.

14. Xu, Z.; Gao, C. *In Situ* Polymerization Approach to Graphene-Reinforced Nylon-6 Composites. *Macromolecules* **2010**, *43*, 6716–6723.

15. He, H. K.; Gao, C. General Approach to Individually Dispersed, Highly Soluble, and Conductive Graphene Nanosheets Functionalized by Nitrene Chemistry. *Chem. Mater.* **2010**, *22*, 5054–5064.

16. Kan, L. Y.; Xu, Z.; Gao, C. General Avenue to Individually Dispersed Graphene Oxide-Based Two-Dimensional Molecular Brushes by Free Radical Polymerization. *Macromolecules* **2011**, *44*, 444–452.

17. Xu, Z.; Gao, C. Aqueous Liquid Crystals of Graphene Oxide. *ACS Nano* **2011**, *5*, 2908–2915.

18. Xu, Z.; Gao, C. Graphene Chiral Liquid Crystals and Macroscopic Assembled Fibres. *Nat. Commun.* **2011**, *2*, 571.

19. Kim, J. E.; Han, T. H.; Lee, S. H.; Kim, J. Y.; Ahn, C. W.; Yun, J. M.; Kim, S. O. Graphene Oxide Liquid Crystals. *Angew. Chem., Int. Ed.* **2011**, *50*, 3043–3047.

20. Dan, B.; Behabtu, N.; Martinez, A.; Evans, J. S.; Kosynkin, D. V.; Tour, J. M.; Pasquali, M.; Smalyukh, I. I. Liquid Crystals of Aqueous, Giant Graphene Oxide Flakes. *Soft Matter* **2011**, *7*, 11154–11159.

21. Aboutalebi, S. H.; Gudarzi, M. M.; Zheng, Q. B.; Kim, J. K. Spontaneous Formation of Liquid Crystals in Ultralarge Graphene Oxide Dispersions. *Adv. Funct. Mater.* **2011**, *21*, 2978–2988.

22. Dikin, D. A.; Stankovich, S.; Zimney, E. J.; Piner, R. D.; Dommett, G. H.; Evmenenko, G.; Nguyen, S. T.; Ruoff, R. S. Preparation and Characterization of Graphene Oxide Paper. *Nature* **2007**, *448*, 457–460.

23. Dong, Z. L.; Jiang, C. C.; Cheng, H. H.; Zhao, Y.; Shi, G. Q.; Lan, J.; Qu, L. T. Facile Fabrication of Light, Flexible and Multifunctional Graphene Fibers. *Adv. Mater.* **2012**, *24*, 1856–1861.

24. Xu, Y. X.; Sheng, K. X.; Li, C.; Shi, G. Q. Self-Assembled Graphene Hydrogel *via* a One-Step Hydrothermal Process. *ACS Nano* **2010**, *4*, 4324–4330.

25. Zhang, X. T.; Sui, Z. Y.; Xu, B.; Yue, S. F.; Luo, Y. J.; Zhan, W. C.; Liu, B. Mechanically Strong and Highly Conductive Graphene Aerogel and Its Use as Electrodes for Electrochemical Power Sources. *J. Mater. Chem.* **2011**, *21*, 6449–6497.

26. Tang, Z. H.; Shen, S. L.; Zhuang, J.; Wang, X. Noble-Metal-Promoted Three-Dimensional Macroassembly of Single-Layered Graphene Oxide. *Angew. Chem., Int. Ed.* **2010**, *49*, 4603–4607.

27. Chen, W. F.; Yan, L. F. *In Situ* Self-Assembly of Mild Chemical Reduction Graphene for Three-Dimensional Architectures. *Nanoscale* **2011**, *3*, 3132–3137.

28. Wang, J.; Ellsworth, M. W. Graphene Aerogels. *ECS Trans.* **2009**, *19*, 241–247.

29. Estevez, L.; Kelarakis, A.; Gong, Q. M.; Da'as, E. H.; Giannelis, E. P. Multifunctional Graphene/Platinum/Nafion Hybrids *via* Ice Templating. *J. Am. Chem. Soc.* **2011**, *133*, 6122–6125.

30. Worsley, M. A.; Pauzauskie, P. J.; Olson, T. Y.; Biener, J.; Satcher, J. H., Jr.; Baumann, T. F. Synthesis of Graphene Aerogel with High Electrical Conductivity. *J. Am. Chem. Soc.* **2010**, *132*, 14067–14069.

31. Hummers, W. S.; Offeman, R. E. Preparation of Graphitic Oxide. *J. Am. Chem. Soc.* **1958**, *80*, 1339.

32. Michot, L. J.; Bihannic, I.; Maddi, S.; Funari, S. S.; Baravian, C.; Levitz, P.; Davidson, P. Liquid-Crystalline Aqueous Clay Suspensions. *Proc. Natl. Acad. Sci. U.S.A.* **2006**, *103*, 16101–16104.

33. Gabriel, J. C. P.; Camerel, F.; Lemaire, B. J.; Desvaux, H.; Davidson, P.; Batail, P. Swollen Liquid-Crystalline Lamellar Phase Based on Extended Solid-like Sheets. *Nature* **2001**, *413*, 504–508.

34. Zhang, H. F.; Hussain, I.; Brust, M.; Butler, M. F.; Rannard, S. P.; Cooper, A. I. Aligned Two- and Three-Dimensional Structures by Directional Freezing of Polymers and Nanoparticles. *Nat. Mater.* **2005**, *4*, 787–793.

35. Bryning, M. B.; Milkie, D. E.; Islam, M. E.; Hough, L. A.; Kikkawa, J. M.; Yodh, A. G. Carbon Nanotube Aerogels. *Adv. Mater.* **2007**, *19*, 661–664.

36. Bandi, S.; Bell, M.; Schiraldi, D. A. Temperature-Responsive Clay Aerogel–Polymer Composites. *Macromolecules* **2005**, *38*, 9216–9220.

37. Qian, L.; Zhang, H. F. Controlled Freezing and Freeze Drying: A Versatile Route for Porous and Micro-/Nano Structured Materials. *J. Chem. Technol. Biotechnol.* **2011**, *86*, 172–184.

38. Pei, S. F.; Zhao, J. P.; Du, J. H.; Ren, W. C.; Cheng, H. M. Direct Reduction of Graphene Oxide Films into Highly Conductive and Flexible Graphene Films by Hydrohalic Acids. *Carbon* **2010**, *48*, 4466–4474.

39. Guo, F.; Kim, F.; Han, T. H.; Shenoy, V. B.; Huang, J. X.; Hurt, R. H. Hydration-Responsive Folding and Unfolding in Graphene Oxide Liquid Crystal Phases. *ACS Nano* **2011**, *5*, 8019–8025.

40. Gabriel, J. C. P.; Davidson, P. New Trends in Colloidal Liquid Crystals Based on Mineral Moieties. *Adv. Mater.* **2000**, *12*, 9–20.

41. Ko, H.; Tsukruk, V. V. Liquid-Crystalline Processing of Highly Oriented Carbon Nanotubes Arrays for Thin-Film Transistors. *Nano Lett.* **2006**, *6*, 1443–1448.

42. Lu, L. H.; Chen, W. Large-Scale Aligned Carbon Nanotubes from Their Purified, Highly Concentrated Suspension. *ACS Nano* **2010**, *4*, 1042–1048.

43. Vigolo, B.; Pénicaud, A.; Coulon, C.; Sauder, C.; Pailler, R.; Journet, C.; Bernier, P.; Poulin, P. Macroscopic Fibers and Ribbons of Oriented Carbon Nanotubes. *Science* **2000**, *290*, 1331–1334.

44. Chen, Z. P.; Ren, W. C.; Gao, L. B.; Liu, B. L.; Pei, S. F.; Cheng, H. M. Three-Dimensional Flexible and Conductive Interconnected Graphene Networks Grown by Chemical Vapour Deposition. *Nat. Mater.* **2011**, *10*, 424–428.

45. Korkut, S.; Roy-Mayhew, J. D.; Dabbs, D. M.; Milius, D. L.; Aksay, I. A. High Surface Area Tapes Produced with Functionalized Graphene. *ACS Nano* **2011**, *5*, 5214–5222.

46. Gui, X. C.; Wei, J. Q.; Wang, K. L.; Cao, A. Y.; Zhu, H. W.; Jia, Y.; Shu, Q. K.; Wu, D. H. Carbon Nanotubes Sponges. *Adv. Mater.* **2010**, *22*, 617–621.

47. Yang, S. B.; Feng, X. L.; Wang, L.; Tang, K.; Maier, J.; Müllen, K. Graphene-Based Nanosheets with a Sandwich Structure. *Angew. Chem., Int. Ed.* **2010**, *49*, 4795–4799.

48. Bolotin, K. I.; Sikes, K. J.; Hone, J.; Stormer, H. L.; Kim, P. Temperature-Dependent Transport in Suspended Graphene. *Phys. Rev. Lett.* **2008**, *101*, 096802.

49. Peng, H. S. Aligned Carbon Nanotube/Polymer Composite Films with Robust Flexibility, High Transparency, and Excellent Conductivity. *J. Am. Chem. Soc.* **2008**, *130*, 42–43.

50. Mott, S. N. *Conduction in Non-crystalline Materials*; Clarendon: Oxford, 1987.

51. Jin, M. H.; Jeong, H. K.; Yu, W. J.; Bae, D. J.; Kang, B. R.; Lee, Y. H. Graphene Oxide Thin Film Field Effect Transistors without Reduction. *J. Phys. D: Appl. Phys.* **2009**, *42*, 135109.

52. Kim, H.; Vural, M.; Islam, M. F. Single-Walled Carbon Nanotube Aerogel-Based Elastic Conductors. *Adv. Mater.* **2011**, *23*, 2865–2869.

53. Worsley, M. A.; Kucheyev, S. O.; Kuntz, J. D.; Hamza, A. V.; Satcher, J. H., Jr.; Baumann, T. F. Stiff and Electrically Conductive Composites of Carbon Nanotube Aerogel and Polymers. *J. Mater. Chem.* **2009**, *19*, 3370–3372.

54. Lu, X. Q.; Qi, H. T.; Zhang, X. F.; Xue, Z. H.; Jin, J.; Zhou, X. B.; Liu, X. H. Highly Dispersive Ag Nanoparticles on Functionalized Graphene for an Excellent Eletrochemical Sensor of Nitroaromatic Compounds. *Chem. Commun.* **2011**, *47*, 12494–12496.

55. Yoo, E. J.; Okata, T.; Akita, T.; Kohyama, M.; Nakamura, J.; Honma, I. Enhanced Electrocatalytic Activity of Pt Sub-nanoclusters on Graphene Nanosheet Surface. *Nano Lett.* **2009**, *9*, 2255–2259.

ARTICLE